

A three-dimensional two-hemisphere model for unmanned aerial vehicle multiple-input multiple-output channels

Zixu Su¹  | Wei Chen¹ | Changzhen Li^{2,3} | Junyi Yu⁴ | Guojiao Gong² | Zixin Wang²

¹School of Automation, Wuhan University of Technology, Wuhan, China

²School of Information Engineering, Wuhan University of Technology, Wuhan, China

³Hubei Key Laboratory of Broadband Wireless Communication and Sensor Networks, Wuhan University of Technology, Wuhan, China

⁴Beijing MetaRadio Technologies Co. Ltd, Beijing, China

Correspondence

Changzhen Li, School of Information Engineering, Wuhan University of Technology, Wuhan, China.
Email: changzhen.li@whut.edu.cn

Funding information

National Natural Science Foundation of China, Grant/Award Number: 52102399; The Fundamental Research Funds for the Central Universities, Grant/Award Number: no. 2022IVA039

Abstract

The application of unmanned aerial vehicles (UAVs) has recently attracted considerable interest in various areas. A three-dimensional multiple-input multiple-output concentric two-hemisphere model is proposed to characterize the scattering environment around a vehicle in an urban UAV-to-vehicle communication scenario. Multipath components of the model consisted of line-of-sight and single-bounced components. This study focused on the key parameters that determine the scatterer distribution. A time-variant process was used to analyze the nonstationarity of the proposed model. Vital statistical properties, such as the space–time–frequency correlation function, Doppler power spectral density, level-crossing rate, average fade duration, and channel capacity, were derived and analyzed. The results indicated that with an increase in the maximum scatter radius, the time correlation and level-crossing rate decreased, the frequency correlation function had a faster downward trend, and average fade duration increased. In addition, with the increase of concentration parameter, the time correlation, space correlation, and level-crossing rate increased, average fade duration decreased, and Doppler power spectral density became flatter. The proposed model was compared with current geometry-based stochastic models (GBSMs) and showed good consistency. In addition, we verified the nonstationarity in the temporal and spatial domains of the proposed model. These conclusions can be used as references in the design of more reasonable communication systems.

KEYWORDS

channel modeling, MIMO channel, statistical properties, UAV communication

1 | INTRODUCTION

In recent years, the application of unmanned aerial vehicles (UAVs) has attracted extensive attention because of their important roles in many scenarios, such as real-time

monitoring, forest fires, and emergency rescue. Therefore, it is important to have a deep understanding of UAV communications to establish more accurate channel models.

Existing UAV channel models can be classified as deterministic, nongeometrical stochastic (NGSMs) [1] and

geometry-based stochastic models (GBSMs). Deterministic models require extensive geographical data, such as the locations, sizes, and dielectric parameters of all scattering materials in specific scenarios. Thus, deterministic models yield high accuracy and complexity. NGSMs obtain the statistical distribution of channel parameters through extensive channel measurements, which means NGSMs require sophisticated channel systems and signal processing.

Compared with NGSMs, GBSMs reduce complexity considerably by assuming that the distribution of scatterers follows geometrical properties. The geometric models for UAV communication systems are diverse. Yan and others [2] conducted a comprehensive survey of UAV communication channel modeling. This survey focused on reviewing air-to-ground, ground-to-ground, and air-to-air channel measurements and modeling for UAV communication in various scenarios.

One of the common GBSMs is the cross-section of an ellipsoid with the transmitter (Tx) and receiver (Rx) as the foci and the ground [3–6]. In Mao and others [6], the proposed geometrical model was applied to characterize a UAV air-to-air channel in which the Markov birth–death process was introduced to describe the evolution of clusters. The space–time correlation function (STCF), Doppler power spectrum density (DPSD), root-mean-square delay spread, and stationary interval were analyzed. The simulation results showed that the UAV velocities, motion directions, and carrier frequencies have a significant impact on statistical properties. The model in Change and others [4] was proposed for low-altitude UAV-to-ground scenarios. In this model, an elliptical cylinder represents the distant scattering region, whereas a cylinder around the Rx was constructed to describe the nearby scattering region. The effectiveness of the model was verified by comparing simulation and measurement results.

In channel modeling of UAV communication, the cylindrical model is also general. A coaxial double-cylinder model was proposed in Ma and others [7], assuming that distant and near scatterers are distributed on the outer and inner cylinder surfaces, respectively. The bottom part of the cylinder was used to simulate ground-moving scatterers. A two-state Markov model was introduced to describe the evolution of the clusters. In Ma and others [8], a cylindrical model was applied to an air-to-air communication scenario. A three-dimensional (3D) Markov mobility model was used to characterize the movement of the UAV. The numerical results show that the impact of the vertical movement of the UAV on the time correlation function is greater than that of the horizontal movement. The model proposed in Ma and others [9] was similar to that proposed in [8]. Different movement scenarios of the UAV were selected, which show that the variation in the velocity and moving direction of the UAV will have an obvious impact

on the statistical properties. In Cheng and others [10], a double-cylindrical model was proposed to simulate the distribution of scatterers around a UAV and base station on the ground. By analyzing the STCF, DPSD, level-crossing rate (LCR), and average fade duration (AFD), it was found that parameters, such as moving direction and height, have a significant impact on the channel characteristics. Based on the cylindrical model in Lian and others [11], a two-state continuous-time Markov process was introduced to simulate the dynamic properties of scatterers. The space–time–frequency correlation functions were derived by considering the survival probabilities of scatterers.

Spherical and hemispherical models are also commonly used in UAV communication channel modeling [12–17]. Bian and others [12] combine a two-cylinder model and an aeronautic random mobility model to describe the temporal nonstationarity of the channel. These results provide a reference for designing UAV communication systems. In Jia and others [16], the UAV was assumed to be directly above the vehicle. A hemispherical model was adopted to simulate the scattering environment. In Jiang and others [13], the scatterers were considered to be distributed on the surface of a sphere centered on the Rx. The STCF was deduced and studied analytically in terms of various key factors. It can be concluded that both the movement direction and location of the UAV have significant influences on the channel characteristics. A similar model was used in Jin and others [15].

In Ma and others [17], a two-sphere model was applied to the air-to-air scenario. The two spheres simulated the scattering environments near the Rx and Tx. This demonstrates that the moving directions, velocities of the UAVs, and antenna spacing can affect statistical properties. In Yuan and others [14], a hemispherical model was used to simulate a scattering environment near a ground vehicle.

Related research has also been conducted on channel modeling and characteristic analysis for UAV communication scenarios, such as air-to-sea communication [18], UAV array communication [19], and UAV-aided satellite communication [20]. Moreover, earlier studies [21, 22] proposed models for intelligently reflecting surface-assisted UAV multiple-input-multiple-output (MIMO) communication scenarios.

However, the aforementioned models assume that scatterers are distributed on the geometric surface. Nevertheless, the scatterers were distributed in the observable region in several cases. Moreover, these models rarely consider the effect of the scattering radius, which is conducive to the measurement of the effect of the scatterer distribution range on the properties. The time-variant process, which is used to verify the nonstationarity of the channel, was not considered in previous research [3, 7, 8, 14].

The contributions of this study can be summarized as follows:

- A two-hemisphere model with time-variant parameters is proposed to characterize the air-to-vehicle MIMO channel. The proposed GBSM considers the line-of-sight (LoS) and single-bounced (SB) components. Time-variant angular parameters as well as distanced parameters are deduced to describe the dynamic process of the proposed channel.
- In the proposed model, the influences of the maximum scatter radius and concentration parameter on the statistical properties are investigated. The use of the maximum scatter radius and concentration parameter can allow the construction of a suitable scattering distribution. By adjusting these variations, the proposed model can apply to different urban environments.
- The channel characteristics, including the space-time-frequency correlation function (STF-CF), DPSD, LCR, AFD, and channel capacity, are derived and analyzed based on the proposed time-variant channel model. Some valuable observations and conclusions are presented.

The remainder of this paper is organized as follows. In Section 2, a two-hemisphere model is proposed for the air-to-vehicle MIMO channel. Theoretical expressions of the statistical properties are presented in Section 3. The numerical results are discussed in Section 4, and conclusions are drawn in Section 5.

2 | GEOMETRY-BASED MODEL FOR UAV CHANNEL

In our considerations, the UAV which contained Tx was assumed to move freely in 3D space, whereas the vehicle which contained the Rx moves on a horizontal xy plane, as shown in Figure 1. Owing to the large height of the UAV, the effect of scattering around the UAV was negligible. The distributions of near (such as nearby vehicles

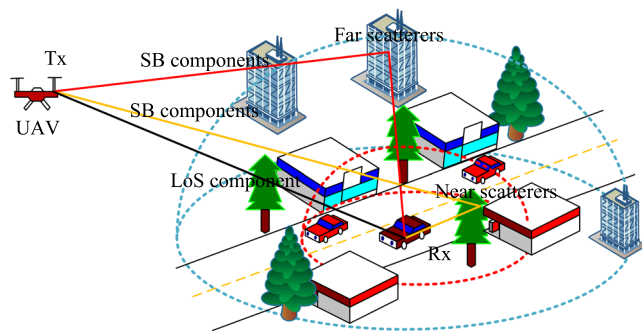


FIGURE 1 Unmanned aerial vehicle (UAV)-to-vehicle propagation model.

and trees) and far (such as buildings) scatterers around the vehicle, modeled by the inner and outer hemispheres, are considered in the urban scenario. Observable scatterers are distributed between the inner and outer hemispheres. According to the geometric models shown in Figure 2, the main geometric variables in the model are defined and listed in Table 1.

In the proposed model, the height of Tx is H_T . The horizontal distance between Tx and Rx is D . The velocities

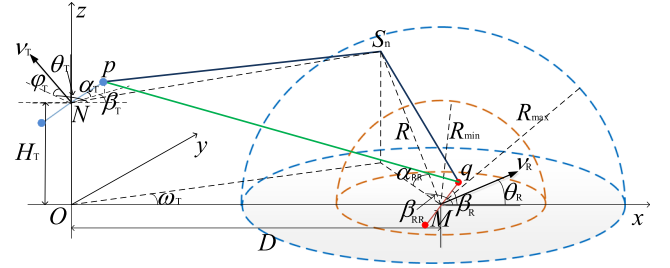


FIGURE 2 Geometry-based stochastic model (GBSM) of the proposed UAV multiple-input-multiple-output (MIMO) channel.

TABLE 1 Definition of geometric variables.

Variable symbols	Geometric variables
Velocities of transmitter (Tx), receiver (Rx)	v_T, v_R
Azimuthal angle of Tx, Rx	θ_T, θ_R
Elevation angle of Tx	ϕ_T
Angle between Tx and Rx antenna arrays and positive direction of x -axis	β_T, β_R
Angle between Tx antenna array and xy plane	α_T
Distance between adjacent antenna spaces of Tx and Rx	δ_T, δ_R
Radii of the inner and outer hemispheres	R_{\min}, R_{\max}
Heights of Tx, Rx	H_T, H_R
Horizontal distance between Tx and Rx	D
Number of scatterers in the area between the two hemispheres	N
Scatterer passed by the n th single bounce path	S_n
Azimuthal and elevation angles of the n th single bounce path on the location of vehicle	α_{RR}, β_{RR}
Azimuthal angle of departure (AAoD) and elevation angle of departure (EAoD) of n th single bounce path	γ_T, ω_T
Azimuthal angle of arrival (AAoA) and elevation angle of arrival (EAoA) of the n th single bounce path	γ_R, ω_R
Distance between S_n and Rx	R
Projection of N on the xy plane	O

and azimuthal angles of the Tx and Rx are labeled as V_T and V_R and θ_T and θ_R , respectively. The elevation angle of Tx was ϕ_T . The orientations of Tx and Rx antenna arrays relative to the positive direction of the x -axis are denoted by β_T and β_R , respectively, whereas the orientation of Tx antenna array relative to the xy plane is denoted by α_T . Both the inner and outer hemispheres are centered on the Rx, with radii R_1 and R_2 . We assume that N scatterers are distributed in the area between the two hemispheres. The n th path formed by a single bounce is denoted as S_n . The azimuthal and elevation angles of the n th scatterer centered at the vehicle location are α_{RR} and β_{RR} , respectively. The AAoD and the EAoD of the n th SB path are γ_T and ω_T . The distance between S_n and the Rx is R . The projection of N onto the xy plane corresponds to the coordinate origin O . In this study, uniform linear antenna arrays are deployed on the Tx and Rx. The distances between adjacent antenna spaces of Tx and Rx are denoted by δ_T and δ_R .

We consider the p th antenna of the transmitting array and the q th antenna of the receiving array as the research targets. The MIMO channel is described by a $M_T \times M_R$ matrix $H(t) = [h_{ij}(t)]_{M_T \times M_R}$. To simplify, we define $k_p = (M_T - 2p + 1)/2$, $k_q = (M_R - 2q + 1)/2$.

2.1 | Time-variant transfer function

In the proposed model, the LoS path extended from the p th antenna of the transmitting array to the q th antenna of the receiving array. The SB path extended from the p th antenna of the transmitting array to the q th antenna of the receiving array via scattering from n th scatterers. The time-variant transfer function at time point t can be written as a superposition of the LoS and SB components, as follows:

$$H_{pq}(t, f) = H_{pq}^{\text{LoS}}(t, f) + H_{pq}^{\text{SB}}(t, f), \quad (1)$$

where f denotes frequency. $H_{pq}^{\text{LoS}}(t, f)$ and $H_{pq}^{\text{SB}}(t, f)$ are the time-variant transfer functions of LoS and SB components, respectively, as expressed in (2) and (3).

$$H_{pq}^{\text{LoS}}(t, f) = \sqrt{\frac{K\Omega_{pq}}{K+1}} e^{j\phi_1 - j2\pi\epsilon_{pq}/\lambda} e^{j2\pi f d_{\text{LoS}}(t) - j2\pi f \tau_{pq}(t)}, \quad (2)$$

$$H_{pq}^{\text{SB}}(t, f) = \sqrt{\frac{\Omega_{pq}}{K+1}} \lim_{N \rightarrow \infty} \frac{1}{\sqrt{N}} \sum_{n=1}^N e^{j\phi - j2\pi(\epsilon_{pS_n} + \epsilon_{S_nq})/\lambda} e^{j2\pi f d(t) - j2\pi f \tau_{S_n}(t)}, \quad (3)$$

where λ denotes the wavelength, K denotes the Rician factor, and Ω_{pq} denotes the total power received. Phases

ϕ_1 and ϕ are independent random variables with uniform distributions in the interval $[-\pi, \pi)$. Owing to the time-variant property of the proposed model, the angular and distanced parameters at different time points were considered.

The complex channel impulse response $h_{pq}(t)$ from the p th antenna of the transmitting array to the q th antenna of the receiving array is a superposition of the LoS component $h_{pq}^{\text{LoS}}(t)$ and SB component $h_{pq}^{\text{SB}}(t)$, which can be expressed as

$$h_{pq}(t) = h_{pq}^{\text{LoS}}(t) + h_{pq}^{\text{SB}}(t), \quad (4)$$

where

$$h_{pq}^{\text{LoS}}(t) = \sqrt{\frac{K\Omega_{pq}}{K+1}} e^{j\phi_1 - j2\pi\epsilon_{pq}/\lambda} e^{j2\pi f d_{\text{LoS}}(t)}, \quad (5)$$

$$h_{pq}^{\text{SB}}(t) = \sqrt{\frac{\Omega_{pq}}{K+1}} \lim_{N \rightarrow \infty} \frac{1}{\sqrt{N}} \sum_{n=1}^N e^{j\phi - j2\pi(\epsilon_{pS_n} + \epsilon_{S_nq})/\lambda} e^{j2\pi f d(t)}. \quad (6)$$

Based on the motions of the Tx and Rx, the channel changes constantly. The assumed scattering environment around the Rx exhibits negligible changes over time. Figure 3 shows the plane projection of the movement process. The location of the projection of the UAV moved from O to O_1 , whereas the location of the vehicle moved from M to M_1 during time t . The relevant angular and distance parameters are deduced as follows:

The height of the UAV changes over time as follows:

$$H_T(t) = H_T + v_T t \sin \phi_T. \quad (7)$$

The deviation angle is expressed as

$$\mu = \arctan \left(\frac{v_R t \sin \theta_R - v_T \sin \theta_T \cos \varphi_T}{D + v_R t \cos \theta_R - v_T \cos \theta_T \cos \varphi_T} \right). \quad (8)$$

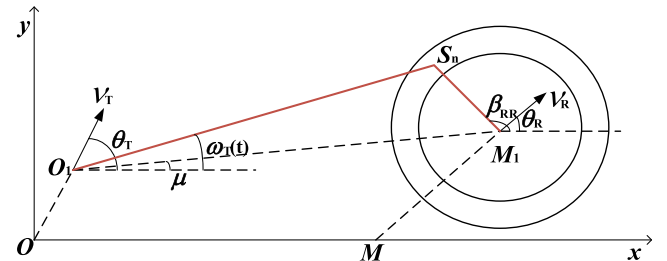


FIGURE 3 Planar projection of the movement process for unmanned aerial vehicle (UAV)-to-vehicle multiple-input-multiple-output (MIMO) channel.

The distance from O_1 to M_1 can be calculated as follows:

$$\epsilon_{O_1M_1} = (D + v_R t \cos \theta_R - v_T \cos \theta_T \cos \phi) \sec \mu. \quad (9)$$

For the LoS path, $\epsilon_{pq}(t)$ denotes the distance from p to q , which can be calculated as

$$\epsilon_{pq}(t) = \sqrt{A^2 + B^2 + C^2}, \quad (10)$$

where

$$\begin{aligned} A &= D + v_R t \cos \theta_R + k_q \delta_R \cos \beta_R \\ &\quad - v_T t \cos \varphi_T \cos \theta_T - k_p \delta_T \cos \alpha_T \cos \beta_T, \\ B &= v_R t \sin \theta_R + k_q \delta_R \sin \beta_R \\ &\quad - v_T t \cos \varphi_T \sin \theta_T - k_p \delta_T \cos \alpha_T \sin \beta_T, \\ C &= H_T(t) + k_p \delta_T \sin \alpha_T. \end{aligned} \quad (11)$$

Thus, the delay $\tau_{pq}(t)$ can be calculated as $\tau_{pq}(t) = \epsilon_{pq}(t)/c$ (where c is the speed of light).

The time-variant Doppler $f_{d,LoS}(t)$ of the LoS path at time t can be calculated as

$$\begin{aligned} f_{d,LoS}(t) &= \frac{v_T(t)}{\lambda} (\cos(\mu - \theta_T) \cos(\omega_{LoS}) \cos \phi_T \\ &\quad + \sin(\omega_{LoS}) \sin \phi_T) \\ &\quad + \frac{v_R}{\lambda} \cos(\mu + \pi - \theta_R) \cos(\omega_{LoS}), \end{aligned} \quad (12)$$

where $\omega_{LoS} = \arctan(H_T(t)/\epsilon_{O_1M_1})$. We define the n th scatterer as $S_n(t)$ at time t . AAoD and EAoD can be expressed as

$$\omega_T(t) = \arctan\left(\frac{\omega_{num}}{\omega_{den}}\right), \quad (13)$$

$$\gamma_T(t) = -\arctan\left(\frac{H_T(t) - R \sin \alpha_{RR}}{\gamma_{den}}\right), \quad (14)$$

where

$$\begin{aligned} \omega_{num} &= R \cos \alpha_{RR} \sin \beta_{RR} + v_R t \sin \theta_R \\ &\quad - v_T \sin \theta_T \cos \phi_T, \\ \omega_{den} &= D + R \cos \alpha_{RR} \cos \beta_{RR} + v_R t \cos \theta_R \\ &\quad - v_T \cos \theta_T \cos \phi_T, \\ \gamma_{den} &= \sqrt{\epsilon_{O_1M_1}^2 + G^2 - 2\epsilon_{O_1M_1} G \cos(\pi + \mu - \beta_{RR})} \\ G &= R \cos \alpha_{RR}. \end{aligned}$$

The time-variant Doppler signal of the SB path at time t , denoted by $f_d(t)$, can be calculated as

$$\begin{aligned} f_d(t) &= \frac{v_T}{\lambda} (\cos(\omega_T(t) - \theta_T) \cos \gamma_T(t) \cos \varphi_T \\ &\quad + \sin \gamma_T(t) \sin \varphi_T) + \frac{v_R}{\lambda} \cos(\theta_R - \beta_{RR}) \cos \alpha_{RR}. \end{aligned} \quad (15)$$

For the SB path, $\epsilon_{p,S_n(t)}$ and $\epsilon_{S_n(t),q}$ are the distances from p to $S_n(t)$ and $S_n(t)$ to q , respectively, as follows:

$$\begin{aligned} \epsilon_{p,S_n(t)} &= \\ &\sqrt{E^2 + F^2 + (H_T(t) + k_p \delta_T \sin \alpha_T - R \sin \alpha_{RR})^2}, \end{aligned} \quad (16)$$

where

$$\begin{aligned} E &= D + v_R t \cos \theta_R + R \cos \alpha_{RR} \cos \beta_{RR} \\ &\quad - v_T t \cos \varphi_T \cos \theta_T - k_p \delta_T \cos \alpha_T \cos \beta_T, \\ F &= v_R t \sin \theta_R + R \cos \alpha_{RR} \sin \beta_{RR} \\ &\quad - v_T t \cos \varphi_T \sin \theta_T - k_p \delta_T \cos \alpha_T \sin \beta_T. \end{aligned}$$

The distance from $S_n(t)$ to q can be calculated as

$$\begin{aligned} \epsilon_{S_n(t),q} &= \\ &\sqrt{R^2 + (k_q \delta_R)^2 - 2R \cos \alpha_{RR} k_q \delta_R \cos(\beta_{RR} - \beta_R)}. \end{aligned} \quad (17)$$

Thus, the delay $\tau_{S_n(t)}$ from p to $S_n(t)$ and q can be calculated as $\tau_{S_n(t)} = (\epsilon_{p,S_n(t)} + \epsilon_{S_n(t),q})/c$.

As the number of scatterers approaches infinity, the exact location of the scatterers is determined by the angle and radius. We assumed that the two continuous random variables that determine the angles of the scatterers have a joint probability density function. In this study, the von Mises–Fisher probability density function was used to describe the probability of a scatterer at a random point on the surface of the hemisphere at a fixed radius. At random joint angles, the von Mises–Fisher probability density function is described as

$$\begin{aligned} f(\alpha_{RR}, \beta_{RR}) &= \\ &\frac{k_R \cos \alpha_{RR}}{4\pi \sinh(k_R)} e^{k_R [\cos \alpha_u \cos \alpha_{RR} \cos(\beta_{RR} - \beta_u) + \sin \alpha_u \sin \alpha_{RR}]} \end{aligned} \quad (18)$$

where $\alpha_{RR} \in [0, \pi/2)$ and $\beta_{RR} \in [-\pi, \pi)$ are the elevation and azimuthal angles of the scatterer, respectively. $\alpha_u \in [0, \pi/2)$ and $\beta_u \in [-\pi, \pi)$ are the statistical mean values of the elevation and azimuthal angles of the scatterer, respectively. The parameter k_R controls the degree of concentration of scatterers around the statistical mean value. As the value of k_R increases, the tighter its distribution around the statistical mean value of the scatterers.

The probability distributions of the far and near scatterers are not the same because of differences in the spatial distribution of buildings. Thus, we adopted a truncated log-normal distribution to describe the probability density of scatterers with different radii, which can be expressed as follows:

$$h(R) = \frac{1}{\sqrt{2\pi}\sigma_R P_R} e^{-\frac{(\ln(R)-R_m)^2}{2\sigma_R^2}} (R_{\min} \leq R \leq R_{\max}), \quad (19)$$

where $P_R = \int_{R_{\min}}^{R_{\max}} h(R) dR$. R_m is the expected radius of the hemisphere and σ_R denotes the standard deviation of radius. Therefore, in the area of the scattering distribution, the probability of any random scatterer is jointly determined by the probabilities of the angle and radius. Furthermore, the model can be applied to various scenarios by adjusting the aforementioned parameters. In an urban scenario, R_{\min} is always influenced by nearby vehicles and street trees, whereas R_{\max} is determined by taller buildings located farther away. Therefore, R_{\min} should be minimized. In empty suburbs, R_{\min} can be increased owing to the lower-density traffic flow and sparser nearby buildings. Nevertheless, in the river scenario, R_{\min} is determined by ships at a distance and buildings on the land. Scatterers are more dispersed. Thus, R_{\min} and R_{\max} are larger and a smaller k_R is selected. Additionally, the parameters in (18) and (19) can change the degree of aggregation and the location of scatterers, which makes the proposed model more accurate for simulations of real-world scattering scenarios.

3 | STATISTICAL PROPERTIES OF GBSM

3.1 | Normalized space-time-frequency correlation function

According to the 3D GBSM described in Section 2, the relevant statistical properties can be derived using (2) and (3). The normalized time-frequency correlation function can be calculated by two different time-variant transfer functions $H_{pq}(t, f)$ and $H_{p'q'}(t, f)$. The time-varying transfer functions from the p th (or p' th) antenna of the transmitting array to the q th (or q' th) antenna of the receiving array can be described as follows.

$$R_{pq,p'q'}(\delta_T, \delta_R, t, \Delta t, \Delta f) = \frac{E(H_{pq}^*(t, f) H_{p'q'}(t + \Delta t, f + \Delta f))}{\sqrt{\text{Var}[H_{pq}(t, f)] \text{Var}[H_{p'q'}(t, f)]}}, \quad (20)$$

where $(\cdot)^*$ denotes complex conjugation, $\text{Var}(\cdot)$ denotes statistical variance, and $E(\cdot)$ denotes the expectation operator. On the basis of (1), (20) can be written as follows:

$$R_{pq,p'q'}(\delta_T, \delta_R, t, \Delta t, \Delta f) = R_{pq,p'q'}^{\text{LoS}}(\delta_T, \delta_R, t, \Delta t, \Delta f) + R_{pq,p'q'}^{\text{SB}}(\delta_T, \delta_R, t, \Delta t, \Delta f), \quad (21)$$

where $R_{pq,p'q'}^{\text{SB}}(\delta_T, \delta_R, t, \Delta t, \Delta f)$ and $R_{pq,p'q'}^{\text{LoS}}(\delta_T, \delta_R, t, \Delta t, \Delta f)$ are the normalized time-frequency correlation functions of the SB and LoS components, respectively. Therefore, by substituting (2) and (3) into (20), the expressions for the normalized time-frequency correlation functions of the SB component and LoS component can be obtained as follows:

$$\begin{aligned} R_{pq,p'q'}^{\text{LoS}}(\delta_T, \delta_R, t, \Delta t, \Delta f) &= \frac{E(H_{pq}^{\text{LoS}}(t, f) * H_{p'q'}^{\text{LoS}}(t + \Delta t, f + \Delta f))}{\sqrt{\text{Var}[H_{pq}^{\text{LoS}}(t, f)] \text{Var}[H_{p'q'}^{\text{LoS}}(t, f)]}} \\ &= K e^{j2\pi(\epsilon_{pq} - \epsilon_{p'q'})/\lambda} e^{j2\pi\Delta f f_{d,\text{LoS}}(t + \Delta t) - j2\pi\Delta f \tau_{\text{LoS}}(t)} e^{j2\pi t(f_{d,\text{LoS}}(t + \Delta t) - f_{d,\text{LoS}}(t))}, \end{aligned} \quad (22)$$

$$\begin{aligned} R_{pq,p'q'}^{\text{SB}}(\delta_T, \delta_R, t, \Delta t, \Delta f) &= \frac{E(H_{pq}^{\text{SB}}(t, f) * H_{p'q'}^{\text{SB}}(t + \Delta t, f + \Delta f))}{\sqrt{\text{Var}[H_{pq}^{\text{SB}}(t, f)] \text{Var}[H_{p'q'}^{\text{SB}}(t, f)]}} \\ &= \lim_{N \rightarrow \infty} \frac{1}{N} \sum_{n=1}^N E(e^{2\pi(\epsilon_{pS_n} + \epsilon_{S_nq})/\lambda} e^{-j2\pi t f_d(t_i) + j2\pi f \tau_{S_n}} \\ &\quad e^{-2\pi(\epsilon_{p'S_n} + \epsilon_{S_nq'})/\lambda} e^{j2\pi(t_i + \Delta t)f_d(t_i + \Delta t) + j2\pi(f + \Delta f)\tau_{S_n}}) \\ &= \int_{-\pi}^{\pi} \int_0^{\pi/2} \int_{R_{\min}}^{R_{\max}} e^{2\pi(\epsilon_{pS_n} + \epsilon_{S_nq} - (\epsilon_{p'S_n} + \epsilon_{S_nq'}))/\lambda} e^{j2\pi t_1(f_d(t_i + \Delta t) - f_d(t_i))} \\ &\quad e^{j2\pi\Delta f f_d(t_i + \Delta t) - j2\pi\Delta f \tau_{S_n}(t)} \\ &\quad f(\alpha_{RR}, \beta_{RR}) h(R) d\alpha_{RR} d\beta_{RR} dR. \end{aligned} \quad (23)$$

3.2 | DPSD

The DPSD is derived by the Fourier transform of time-frequency correlation function $R_{pq,p'q'}(\delta_T, \delta_R, t_i, \Delta t, \Delta f)$ with $t_i = 0$, $\Delta t = 0$, $\Delta f = 0$. Thus, the DPSD can be expressed as

$$S_{pq,p'q'}(f_D) = \int_{-\infty}^{\infty} R_{pq,p'q'}(t, \Delta t) e^{-j2\pi f_D \Delta t} d\Delta t, \quad (24)$$

where f_D is the Doppler frequency. In the proposed model, the DPSD is a superposition of the LoS and SB components.

$$S_{pq,p'q'}(f_D, t) = S_{pq,p'q'}^{\text{LoS}}(f_D, t) + S_{pq,p'q'}^{\text{SB}}(f_D, t). \quad (25)$$

3.3 | Envelope LCR

The LCR is defined as the average number of times the signal envelope passes a certain level value r with a positive/negative slope per unit of time. It is used to describe the statistical rules for the number of fading cycles. Using traditional PDF-based methods, the LCR of the model can be written as [23]

$$L(r) = \frac{2r\sqrt{K+1}}{\pi^2} \sqrt{\frac{b_2 b_0 - b_1^2}{b_0^2}} e^{-K-(K+1)r^2} \int_0^{\frac{\pi}{2}} \cosh \left(2\sqrt{K(K+1)}r \cos \theta \right) \left[e^{-(\chi \sin \theta)^2} + \sqrt{\pi}\chi \sin \theta \text{erf}(\chi \sin \theta) \right] d\theta, \quad (26)$$

where $\cosh(\cdot)$ is the hyperbolic cosine, $\text{erf}(\cdot)$ is the error function, and $\chi = \sqrt{Kb_1^2/(b_0b_2 - b_1^2)}$. Parameters b_0, b_1, b_2 are defined as

$$\begin{aligned} b_0 &= E[h_{pq}^{\text{SB,I}}(t)^2] = E[h_{pq}^{\text{SB,Q}}(t)^2] \\ b_1 &= E[h_{pq}^{\text{SB,I}}(t)\dot{h}_{pq}^{\text{SB,Q}}(t)] = E[h_{pq}^{\text{SB,Q}}(t)\dot{h}_{pq}^{\text{SB,I}}(t)] \\ b_2 &= E[\dot{h}_{pq}^{\text{SB,Q}}(t)^2] = E[\dot{h}_{pq}^{\text{SB,I}}(t)^2], \end{aligned} \quad (27)$$

where $h_{pq}^{\text{SB,I}}(t)$ and $h_{pq}^{\text{SB,Q}}(t)$ are the in-phase and quadrature components of $h_{pq}^{\text{SB}}(t)$, respectively. $\dot{h}_{pq}^{\text{SB,I}}(t)$ and $\dot{h}_{pq}^{\text{SB,Q}}(t)$ are the first derivatives of $h_{pq}^{\text{SB,I}}(t)$ and $h_{pq}^{\text{SB,Q}}(t)$ with respect to time t ,

Based on the derivation of the aforementioned model, substitution of (5) and (6) into (27) b_m ($m = 0, 1, 2, \dots$) can be derived as

$$\begin{aligned} b_m &= \frac{1}{2(K+1)} \int_{-\pi}^{\pi} \int_0^{\frac{\pi}{2}} \int_{R_{\min}}^{R_{\max}} \left(\frac{v_T(t_i)}{\lambda} (\cos(\theta_T(t_i) - \omega_T) \cos \gamma_T \cos \phi_T(t_i) \right. \\ &\quad \left. + \sin \gamma_T \sin \phi_T(t_i)) + \frac{v_R}{\lambda} \cos(\theta_R - \beta_{RR}) \cos \alpha_{RR} \right)^m \\ &\quad f(\alpha_{RR}, \beta_{RR}) h(R) d\alpha_{RR} d\beta_{RR} dR. \end{aligned} \quad (28)$$

Substituting $m = 0, 1, 2$ into (28), b_0, b_1 , and b_2 can be expressed as

$$b_0 = \frac{1}{2(K+1)}, \quad (29)$$

$$\begin{aligned} b_1 &= \frac{1}{2(K+1)} \int_{-\pi}^{\pi} \int_0^{\frac{\pi}{2}} \int_{R_{\min}}^{R_{\max}} \left(\frac{v_T(t_i)}{\lambda} (\cos(\theta_T(t_i) - \omega_T) \right. \\ &\quad \left. \cos \gamma_T \cos \phi_T(t_i) + \sin \gamma_T \sin \phi_T(t_i)) \right. \\ &\quad \left. + \frac{v_R}{\lambda} \cos(\theta_R - \beta_{RR}) \cos \alpha_{RR} \right) \\ &\quad f(\alpha_{RR}, \beta_{RR}) h(R) d\alpha_{RR} d\beta_{RR} dR \end{aligned} \quad (30)$$

$$\begin{aligned} b_2 &= \frac{1}{2(K+1)} \int_{-\pi}^{\pi} \int_0^{\frac{\pi}{2}} \int_{R_{\min}}^{R_{\max}} \left(\frac{v_T(t_i)}{\lambda} (\cos(\theta_T(t_i) - \omega_T) \right. \\ &\quad \left. \cos \gamma_T \cos \phi_T(t_i) + \sin \gamma_T \sin \phi_T(t_i)) \right. \\ &\quad \left. + \frac{v_R}{\lambda} \cos(\theta_R - \beta_{RR}) \cos \alpha_{RR} \right)^2 \\ &\quad f(\alpha_{RR}, \beta_{RR}) h(R) d\alpha_{RR} d\beta_{RR} dR. \end{aligned} \quad (31)$$

3.4 | Envelope AFD

AFD is the average value of the sum of the durations of each segment in which the signal envelope drops below a given level r in a certain statistical time, which can be expressed as

$$T(r) = \frac{1 - Q(\sqrt{2K}, \sqrt{2(K+1)r^2})}{L(r)}, \quad (32)$$

where $Q(\cdot, \cdot)$ is the Marcum Q function.

Based on (32), we observe that the AFD can be derived using LCR.

3.5 | Channel capacity

For the proposed $M_T \times M_R$ MIMO channel, the relationship between the receiving and transmitting-signal vectors can be expressed as [24]

$$y(t) = H(t)s(t) + n(t). \quad (33)$$

where $y(t)$ and $x(t)$ denote the $M_R \times 1$ receiving-signal vector and $M_T \times 1$ transmitting-signal vector, respectively. $n(t)$ denotes an $M_R \times 1$ noise vector. The channel capacity is used to evaluate the maximum error-free information rate that can be transmitted. The proposed model can be used to evaluate the channel capacity of UAV communication. The ergodic channel capacity can be expressed as

$$C = E \left[\log_2 \det \left(I_{M_T} + \frac{SNR}{M_R} HH^H \right) \right] \quad (34)$$

where I_{M_T} denotes an $M_R \times M_R$ identity matrix and the dimensions of the channel matrix H are $M_R \times M_T$. $(\cdot)^H$ denotes the transpose-conjugate operation. The SNR denotes the signal-to-noise ratio. The channel matrix of the multipath components is derived as follows [22],

$$\mathbf{H} = \mathbf{H}^{\text{LoS}} + \mathbf{H}^{\text{SB}}. \quad (35)$$

The conventional Kronecker model assumes no correlation between the receiver and transmit array matrices. The channel matrix can be expressed as [25]

$$\mathbf{H} = \mathbf{R}_R^{\frac{1}{2}} \mathbf{H}_w \mathbf{R}_T^{\frac{1}{2}} \quad (36)$$

where R_T and R_R are the correlation matrices for the Tx and Rx, respectively. \mathbf{H}_w is a $M_T \times M_R$ stochastic matrix with complex independent Gaussian-distributed entries. $(\cdot)^{\frac{1}{2}}$ denotes the square root.

4 | NUMERICAL RESULTS AND ANALYSIS

In this section, the time-variant channel statistical properties are simulated and analyzed based on the proposed model. The autocorrelation function (ACF) (time domain), frequency correlation function (FCF), spatial cross-correlation (SCCF), DPSD, LCR, AFD, and channel capacity were simulated. The acronyms are listed in Table 2. The influence of certain parameters on channel characteristics was explored and analyzed. The simulation parameters were set as follows: $f = 3.5\text{GHz}$, $\alpha_T = \pi/4$, $\beta_T = \pi/3$, $\theta_T(t) = \pi/2$, $\theta_R = \pi/3$, $\phi_T(t) = 5\pi/12$, $\delta_T = \delta_R = \lambda/2$, $k_R = 2$, $v_R = 10\text{m/s}$, $v_T = 20\text{m/s}$, $D = 200\text{m}$, $H_T = 30\text{m}$, $\alpha_u = \pi/12$, $\beta_u = \pi/6$, $R_{\min} = 1\text{m}$, $R_{\max} = 50\text{m}$, $R_m = 3.8\text{m}$, $\sigma_R = 0.4$.

A comparison between the normalized ACF of the proposed model and normalized ACFs in earlier studies [12, 13, 15, 25] is presented in Figure 4. The ACF $R_{pq}(\Delta t)$ can be obtained by setting $\delta_T = 0$, $\delta_R = 0$, $\Delta f = 0$, $p = p'$,

TABLE 2 Table for all acronyms.

Unmanned aerial vehicles	UAV
Three-dimensional	3D
Multiple-input multiple-output	MIMO
Line-of-sight	LoS
Single-bounced	SB
Space-time-frequency correlation function	STF-CF
Doppler power spectrum density	DPSD
Level-crossing rate	LCR
Average fade duration	AFD
Nongeometrical stochastic models	NGSMs
Geometry-based stochastic models	GBSMs
Autocorrelation function (time domain)	ACF
Frequency correlation function	FCF
Spatial cross-correlation function	SCCF

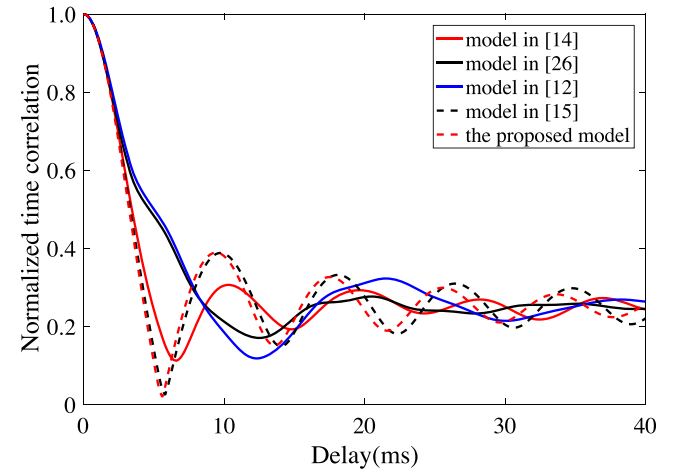


FIGURE 4 Normalized time correlations of the proposed model, model in Jia et al. [13], model in Jia et al. [25], model in Bian et al. [12], and model in Jin et al. [15].

$q = q'$. The model of the sphere in Jia and others [13], cylinder model in Jia and others [25], two-cylinder model in Bian and others [12], and hemisphere model in Jin and others [15] were simulated to verify how reasonable the proposed channel model was. The ACFs of all the models eventually level off at approximately $\frac{K}{K+1}$. The root-mean-square errors of the ACFs of the proposed and existing models are listed in Table 3. From the table listings, it can be concluded that the ACF of the proposed model is more similar to that of the hemisphere model in Jin and others [15] and the sphere model in Jiang and others [13] because the proposed model is based on the improved sphere model. However, there was a considerable difference compared with the cylinder-based model.

TABLE 3 Root-mean-square error between the proposed model and other models.

Comparison model	Root-mean-square error
Sphere model in Jin et al. [15]	0.0582
Cylinder model in Jia et al. [25]	0.1064
Two-cylinder model in Bian et al. [12]	0.1186
Hemisphere model in Jin et al. [15]	0.0244

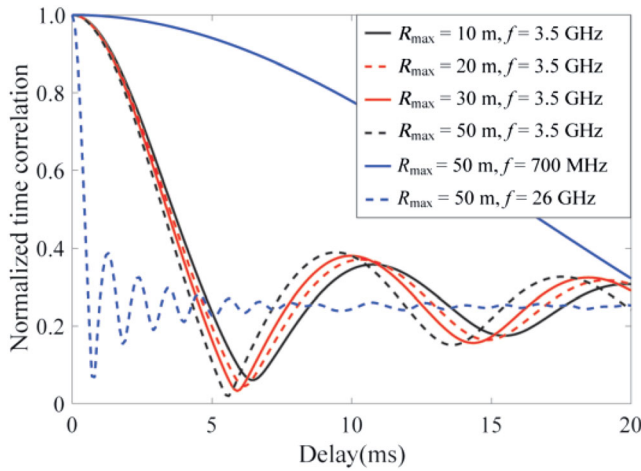


FIGURE 5 Normalized temporal correlations of the proposed model at different maximum scatter radii and frequencies.

Thus, we can speculate that the sphere- and cylinder-based models with the same distribution may simulate two different actual scattering scenarios.

Figure 5 presents the normalized ACF in terms of different frequencies and the maximum scatter radius. When the propagation delay increased, the ACF decreased rapidly and gradually stabilized. In addition, a larger maximum scatter radius leads to a faster downward trend and larger amplitudes, which results from the distribution of scatterers. Thus, the size of the scattering region affects the ACF. Moreover, the ACF exhibits a more rapid downward trend at higher frequencies. Thus, it is crucial to select an appropriate frequency to enhance communication capability.

Figure 6 presents the normalized ACF at different delays and time points. As time increased, the ACF decreased more rapidly and stabilized quickly. In this study, the scattering environment was assumed to be constant around the Rx. Because of the motion of the UAV and vehicle, the orientations of scatterers relative to the UAV changed over time, which leads to channel non-stationarity in the time domain.

Figure 7 shows the ACFs as functions of different concentration parameters k_R ; these represent the spread

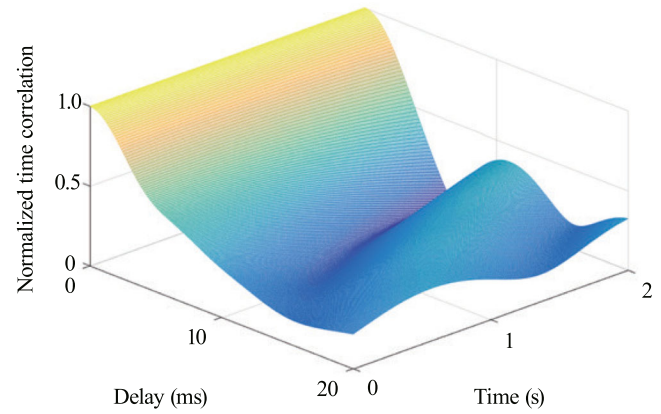


FIGURE 6 Normalized time correlation of the proposed model at different delays and times.

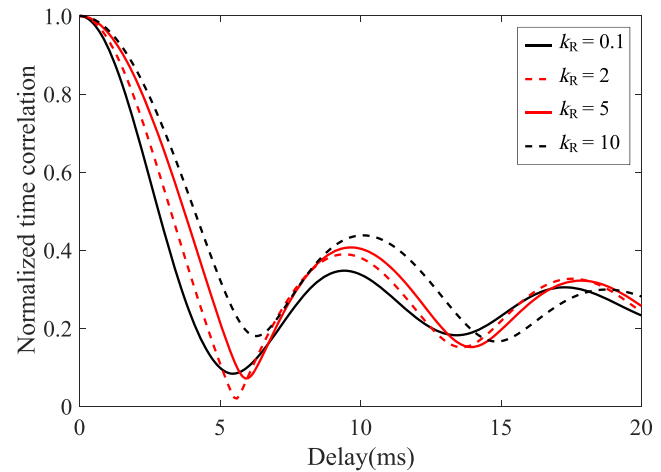


FIGURE 7 Normalized time correlation of the proposed model at different k_R values.

TABLE 4 Coherence time at different k_R values.

k_R	Coherence time (ms)
0.1	3.1
2	3.5
5	4.0
10	4.1

of scatterers around the mean angle. This illustrates that a larger concentration parameter results in a larger ACF. This is because scatterers are more concentrated near the mean angle, thus resulting in a smaller angular distribution range. Thus, environments with more diffuse scatterers generated smaller time correlations. In addition, the coherence time T_c , which describes the maximum transmission time of the signals without distortion, can be estimated. T_c is defined as the first instant at which the ACF decreases below 0.5, as shown in Table 4. We

can conclude that as the distribution of the scatterers becomes more dispersed, the coherence time becomes shorter.

By setting $\delta_R = 0$, $\Delta f = 0$, $\Delta t = 0$, $p = q = 1$, $p' = q' = 2$, the spatial correlation for the antenna spacings of the Tx $R_{pq,p'q'}(\delta_R)$ at different times is illustrated in Figure 8. We note that the normalized space correlation has a slower downward trend and decreases over time, which demonstrates the nonstationarity of the proposed model in the spatial domain. This is because the motions of the Tx and Rx lead to smaller angular spreads relative to those of the Tx. Moreover, the model in Jia and others [13] exhibits a similar trend when the LoS component is considered, thus demonstrating the fact that the proposed model is reasonable.

The spatial correlation of the antenna spacings of Tx with different concentration parameters is shown in Figure 9. Note that a larger k_R leads to a larger spatial correlation in terms of the antenna spacing of the Tx. The factor contributing to this situation is that a larger k_R leads to a concentration of scatterers around the mean angles and results in a reduction in the distribution range of the path difference between different antennas through the same scatterer. Thus, better MIMO performance is derived with more dispersive scatterers.

By setting $\Delta f = 0$, $\Delta t = 0$, $p = q = 1$, $p' = q' = 2$, we can obtain the joint SCCF of antenna spacings of Tx and Rx $R_{pq,p'q'}(\delta_T, \delta_R)$ in Figure 10. The SCCF of the first antenna of Tx and Rx and the second antennas of Tx and Rx were explored. It can be observed that the Tx antenna spacings of Tx exhibit a larger fluctuation than those of the Rx antenna spacings. In an actual scenario, multipath components of the MIMO channel are not always independent, especially when the LoS component exists, which increases the difficulty of antenna deployment. The

correlation function of the proposed model served as a reference for obtaining smaller spatial correlations.

By setting $\delta_T = 0$, $\delta_R = 0$, $\Delta t = 0$, $p = p'$, $q = q'$, we can obtain the FCF for different maximum scatter radii (see Figure 11). The FCF exhibits a slower descent rate and greater amplitude as the maximum scatter radius decreases. This was a result of the influence of the maximum scatter radius on the distribution of scatterers.

Figure 12 shows the simulation results of the LCR for different maximum scatter radii and k_R values. The LCR increases significantly with a decrease in the maximum scatter radius and an increase in k_R . Similarly, the AFD increased with an increase in the maximum scatter radius and a decrease in k_R . Therefore, a stable channel can be obtained by expanding the scattering region and dispersing the scatterers.

Figure 13 studies the simulation results of DPSD for different concentration parameters k_R . It can be observed that when k_R decreases, Doppler decreases. This is because a smaller k_R implies that the angles of scatterers

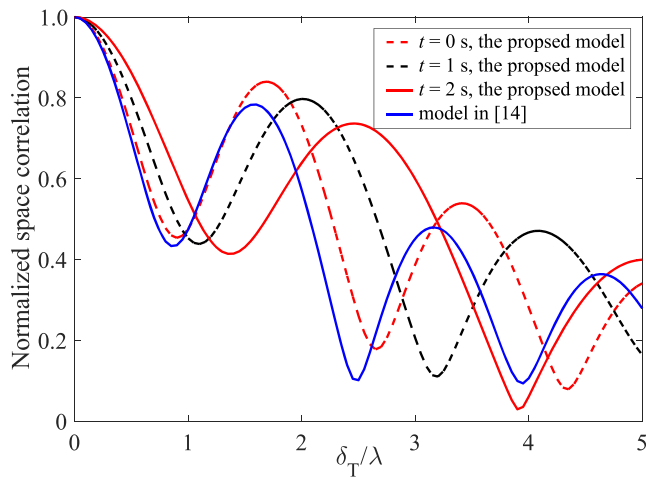


FIGURE 8 Spatial correlation functions of the antenna spacings of the transmitter (Tx) at different times.

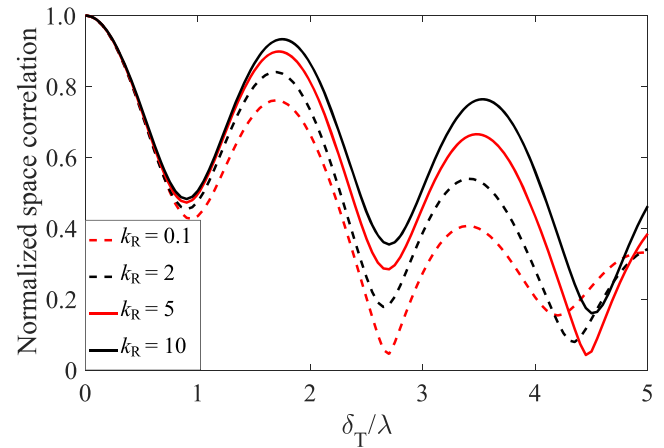


FIGURE 9 Spatial correlation functions of the antenna spacings of the Tx at different k_R values.

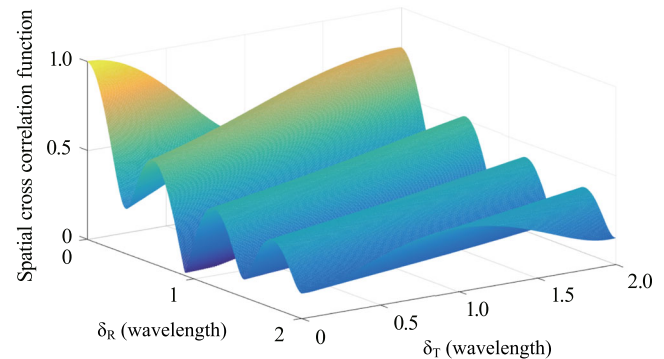


FIGURE 10 Spatial cross-correlation function for different antenna spacings of the Tx and receiver.

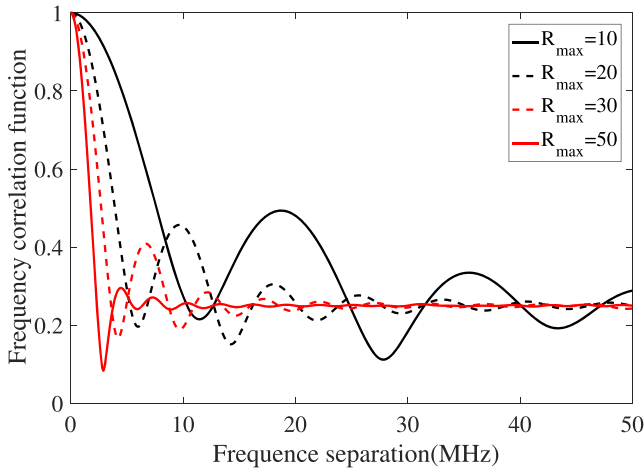


FIGURE 11 Frequency correlation functions for different maximum scatter radii and k_R .

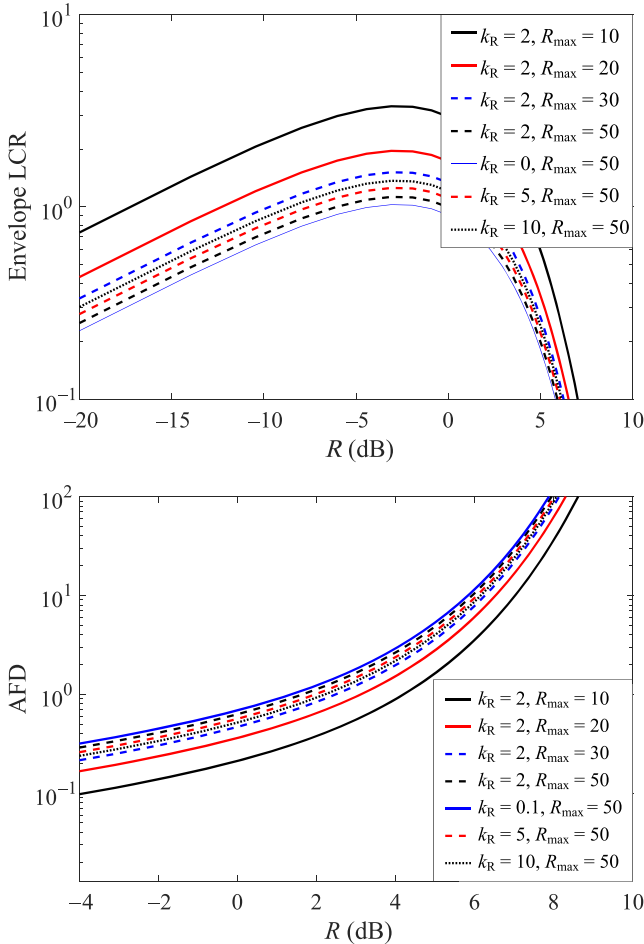


FIGURE 12 Level-crossing rate and average fade duration for different maximum scatter radii and k_R values.

are more well-proportioned, which leads to a more evenly distributed Doppler frequency. Table 5 shows the variance of DPSD of Figure 13. When $k_R = 0.1$, the DPSD

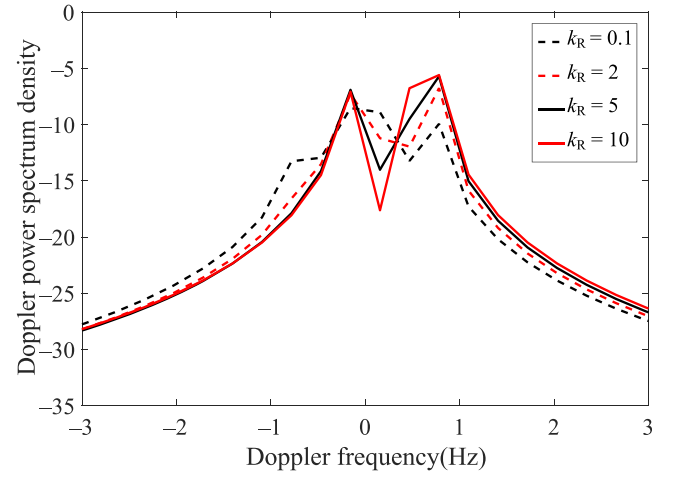


FIGURE 13 Doppler power spectrum density for different k_R values.

TABLE 5 Variance of DPSD.

k_R	Variance
0.1	3.8598
2	4.3873
5	4.7902
10	5.2021

Abbreviation: DPSD, Doppler power spectrum density.

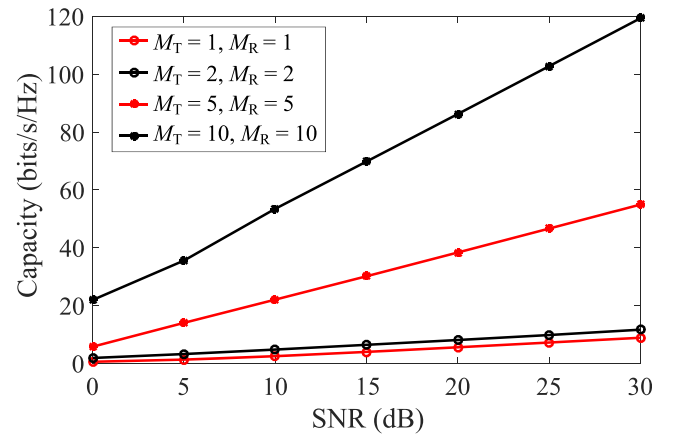


FIGURE 14 Capacity comparison as a function of the signal-to-noise ratio for different numbers of antennas.

is the highest and the variance is the minimum. As k_R increases, the variance tends to increase.

By calculating (34), Figure 14 shows the channel capacity for different numbers of the transmitting and receiving antennas. It is evident that the channel capacity increases as a function of the signal-to-noise ratio. In addition, more antennas deployed on the UAV and vehicle resulted in a larger channel capacity; this finding is

consistent with the conclusions of [26]. Hence, a higher signal-to-noise ratio and more antennas allocated at Tx and Rx can enhance the transmission efficiency of information on the channel.

5 | CONCLUSIONS

In this study, a concentric two-hemisphere model was proposed to characterize a time-variant UAV-to-vehicle 3D MIMO channel. The LoS and SB components in the channel were considered. Based on the proposed model, the effects of the maximum scatter radius and concentration parameter k_R on the statistical characteristics were explored. Statistical properties, including the normalized ACF, SCCF, FCF, LCR, AFD, DPSD, and channel capacity, were derived and analyzed. The results indicated that different maximum scatter radii and concentration parameters had obvious influences on channel characteristics. Moreover, the nonstationarity of the channel in the temporal and spatial domains was demonstrated. Specifically, with an increase in the maximum scatter radius, ACF decreased, FCF exhibited a quicker descent rate, LCR decreased, and AFD increased. In addition, with the increase of k_R , ACF, SCCF, and LCR increased, AFD decreased, and DPSD became flatter. The proposed model was compared with current GBSMs and showed good consistency.

ACKNOWLEDGMENTS

This study was supported by the National Natural Science Foundation of China (grant no. 52102399).

CONFLICT OF INTEREST STATEMENT

The authors declare that there are no conflicts of interest.

ORCID

Zixu Su  <https://orcid.org/0000-0001-5045-6733>

REFERENCES

1. Y. Wang, R. Zhang, B. Li, X. Tang, and D. Wang, *Angular spread analysis and modeling of UAV air-to-ground channels at 3.5 GHz*, (11th International Conference on Wireless Communications and Signal Processing (WCSP), Xian, China), 2019, pp. 1–5.
2. C. Yan, L. Fu, J. Zhang, and J. Wang, *A comprehensive survey on UAV communication channel modeling*, IEEE Access **7** (2019), 107769–107792.
3. H. Chang, J. Bian, C.-X. Wang, Z. Bai, J. Sun, and X. Gao, *A 3d wideband geometry-based stochastic model for UAV air-to-ground channels*, (IEEE Global Communications Conference (GLOBECOM), Abu Dhabi, United Arab Emirates), 2018, pp. 206–212.
4. H. Chang, J. Bian, C.-X. Wang, Z. Bai, and W. Zhou, *A 3d non-stationary wideband GBSM for low-altitude UAV-to-ground V2V MIMO channels*, IEEE Access **7** (2019), 70719–70732.
5. J. Mao, Z. Wei, K. Liu, Z. Cheng, B. Xing, and H. Li, *A 3D air-to-ground channel model based on a street scenario*, (IEEE 6th International Conference on Computer and Communications (ICCC), Chengdu, China), 2020, pp. 1356–1362.
6. X. Mao, C.-X. Wang, and H. Chang, *A 3d non-stationary geometry-based stochastic model for 6G UAV air-to-air channels*, (13th International Conference on Wireless Communications and Signal Processing (WCSP), Chengdu, China), 2021, pp. 1–5.
7. Z. Ma, B. Ai, R. He, and Z. Zhong, *A 3d air-to-air wideband non-stationary channel model of UAV communications*, (IEEE 90th Vehicular Technology Conference (VTC2019-FALL), Honolulu, HI, USA), 2019, pp. 1–5.
8. Z. Ma, B. Ai, R. He, G. Wang, Y. Niu, and Z. Zhong, *A wideband non-stationary air-to-air channel model for UAV communications*, IEEE Trans. Veh. Technol. **69** (2019), no. 2, 1214–1226.
9. Z. Ma, B. Ai, R. He, Z. Zhong, M. Yang, J. Wang, L. Pei, Y. Li, and J. Li, *Three-dimensional modeling of millimeter-wave MIMO channels for UAV-based communications*, (Globecom 2020-2020 IEEE Global Communications Conference, Taipei, Taiwan), 2020, pp. 1–6.
10. X. Cheng, Y. Li, C.-X. Wang, X. Yin, and D. W. Matolak, *A 3-d geometry-based stochastic model for unmanned aerial vehicle MIMO Ricean fading channels*, IEEE Internet Things J. **7** (2020), no. 9, 8674–8687.
11. Z. Lian, Y. Su, Y. Wang, L. Jiang, Z. Zhang, Z. Xie, and S. Li, *A nonstationary 3-D wideband channel model for low-altitude UAV-MIMO communication systems*, IEEE Internet Things J. **9** (2021), no. 7, 5290–5303.
12. J. Bian, C. X. Wang, Y. Liu, J. Tian, J. Qiao, and X. Zheng, *3d non-stationary wideband UAV-to-ground MIMO channel models based on aeronautic random mobility model*, IEEE Trans. Veh. Technol. **70** (2021), no. 11, 11154–11168.
13. R. Jia, Y. Li, X. Cheng, and B. Ai, *3d geometry-based UAV-MIMO channel modeling and simulation*, China Commun. **15** (2018), no. 12, 64–74.
14. K. Jiang, X. Chen, Q. Zhu, W. Zhong, Y. Wang, X. Yu, and B. Chen, *A geometry-based 3d non-stationary UAV-MIMO channel model allowing 3d arbitrary trajectories*, (10th International Conference on Wireless Communications and Signal Processing (WCSP), Hangzhou, China), 2018, pp. 1–6.
15. K. Jin, X. Cheng, X. Ge, and X. Yin, *Three dimensional modeling and space-time correlation for UAV channels*, (IEEE 85th Vehicular Technology Conference (VTC SPRING), Sydney, Australia), 2017, pp. 1–5.
16. Z. Ma, B. Ai, R. He, G. Wang, Y. Niu, M. Yang, J. Wang, Y. Li, and Z. Zhong, *Impact of UAV rotation on MIMO channel characterization for air-to-ground communication systems*, IEEE Trans. Veh. Technol. **69** (2020), no. 11, 12418–12431.
17. Y. Yuan, X. Cheng, C.-X. Wang, D. I. Laurenson, X. Ge, and F. Zhao, *Space-time correlation properties of a 3D two-sphere model for non-isotropic MIMO mobile-to-mobile channels*, (IEEE Global Telecommunications Conference GLOBECOM 2010, Miami, FL, USA), 2010, pp. 1–5.
18. Y. Liu, C.-X. Wang, H. Chang, Y. He, and J. Bian, *A novel non-stationary 6G UAV channel model for maritime communications*, IEEE J. Sel. Areas Commun. **39** (2021), no. 10, 2992–3005.
19. Q. Tang, Z. Wei, S. Chen, and Z. Cheng, *Modeling and simulation of A2G channel based on UAV array*, (IEEE 6th International Conference on Computer and Communications (ICCC), Chengdu, China), 2020, pp. 500–506.

20. L. Hu, Z. Zhang, B. Deng, and W. Zhou, *Channel modeling for UAV-aided leo satellite communication*, (24th International Symposium on Wireless Personal Multimedia Communications (WPMC), Okayama, Japan), 2021, pp. 1–6.
21. Z. Lian, P. Ji, Y. Wang, Y. Su, B. Jin, Z. Zhang, Z. Xie, and S. Li, *Geometry-based UAV-MIMO channel modeling assisted by intelligent reflecting surface*, *IEEE Trans. Veh. Technol.* **71** (2022), 6698–6703.
22. G. Sun, R. He, B. Ai, Z. Ma, P. Li, Y. Niu, J. Ding, D. Fei, and Z. Zhong, *A 3D wideband channel model for RIS-assisted MIMO communications*, *IEEE Trans. Veh. Technol.* **71** (2022), 8016–8029.
23. A. G. Zajic, G. L. Stuber, T. G. Pratt, and S. Nguyen, *Envelope level crossing rate and average fade duration in mobile-to-mobile fading channels*, (IEEE International Conference on Communications, Nanjing, China), 2008, pp. 4446–4450.
24. C.-X. W. Yang and J. Huang, *Comparisons of channel characteristics and capacities of three 5G/B5G wireless channel models*, (IEEE 95th Vehicular Technology Conference, Helsinki, Finland), 2022, pp. 1–5.
25. H. Jia, H. Chen, and Y. Zhang, *3d non-stationary unmanned aerial vehicles' MIMO channel model*, *IET Commun.* **13** (2019), 2941–2945.
26. C. J. Tan, *Comparison and analysis of MIMO channel capacity*, (International Conference on Wireless Communications, Networking and Mobile Computing. IEEE, Shanghai, China), 2007, pp. 299–301.

AUTHOR BIOGRAPHIES



Zixu Su is now a postgraduate student at Wuhan University of Technology. His main research interest is wireless channel modeling.



Wei Chen received his Ph.D. degree in Information and Communication Engineering from the Huazhong University of Science and Technology, Wuhan, China, in 2005. He is currently a Professor and Doctoral Supervisor at the Wuhan University of Technology, Wuhan, China. His current research interests include channel measurement and modeling, massive MIMO technology, millimeter wave

technology, satellite navigation system theory and technology applications, and intelligent traffic control systems.



Changzhen Li received his M.S. and Ph.D. degrees in Engineering, both from Wuhan University of Technology (WUT), Wuhan, China, in 2017 and 2020, respectively. He is currently an Associate Research Fellow with the School of Information Engineering, Wuhan University of Technology, Wuhan, China. His current research interests include radio channel measurements and modeling.



Junyi Yu received his Ph.D. degree in Engineering from Wuhan University of Technology (WUT), Wuhan, China, in 2019. His current research interests include radio channel measurements and modeling.



Guojiao Gong is now a postgraduate student at Wuhan University of Technology. His main research interest is wireless channel modeling.



Zixin Wang is now a postgraduate student at Wuhan University of Technology. His main research interest is wireless channel modeling.

How to cite this article: Z. Su, W. Chen, C. Li, J. Yu, G. Gong, and Z. Wang, *A three-dimensional two-hemisphere model for unmanned aerial vehicle multiple-input multiple-output channels*, *ETRI Journal* **45** (2023), 768–780. DOI [10.4218/etrij.2022-0456](https://doi.org/10.4218/etrij.2022-0456)